

UC Berkeley

UC Berkeley Previously Published Works

Title

Ultrahigh power and energy density in partially ordered lithium-ion cathode materials

Permalink

<https://escholarship.org/uc/item/5dx8t1jc>

Journal

Nature Energy, 5(3)

ISSN

2058-7546

Authors

Ji, H
Wu, J
Cai, Z
et al.

Publication Date

2020-03-01

DOI

10.1038/s41560-020-0573-1

Peer reviewed

**Ultrahigh power and energy density
in partially ordered lithium-ion cathode materials**

Huiwen Ji^{1,2}, Jinpeng Wu^{3,&}, Zijian Cai^{1,2,&}, Jue Liu⁴, Deok-Hwang Kwon^{1,2}, Hyunchul Kim²,
Alexander Urban⁵, Joseph K. Papp⁶, Emily Foley⁷, Yaosen Tian^{1,2}, Mahalingam
Balasubramanian⁸, Haegyeom Kim², Raphaële J. Clément⁷, Bryan D. McCloskey⁶, Wanli Yang³
and Gerbrand Ceder^{1,2,*}

¹*Department of Materials Science and Engineering, University of California Berkeley, Berkeley, CA
94720, USA*

²*Materials Sciences Division, Lawrence Berkeley National Laboratory, Berkeley, CA 94720, USA*

³*The Advanced Light Source, Lawrence Berkeley National Laboratory, Berkeley, CA, USA*

⁴*Neutron Scattering Division, Oak Ridge National Laboratory, Oak Ridge, TN, USA*

⁵*Department of Chemical Engineering, Columbia University, New York, NY, USA*

⁶*Department of Chemical and Biomolecular Engineering, University of California Berkeley, Berkeley, CA
94720, USA*

⁷*Materials Department, University of California Santa Barbara, Santa Barbara, CA 93106, USA*

⁸*X-Ray Science Division, Advanced Photon Source, Argonne National Laboratory Argonne, IL 60439,
USA*

[&]These authors contributed equally.

^{*}gceder@berkeley.edu

Abstract

The rapid market growth of rechargeable batteries requires electrode materials that combine high power and energy and are made from earth-abundant elements. Here we show that combining partial spinel-like cation order and substantial lithium excess enables both dense and fast energy storage. Cation over-stoichiometry and the resulting partial order is used to eliminate phase transitions typical for ordered spinels and enable larger practical capacity, while lithium excess is synergistically used with fluorine substitution to create high lithium mobility. With this strategy, we achieve specific energies greater than 1,100 Wh kg⁻¹ and discharge rates up to 20 A g⁻¹. Remarkably, the cathode materials thus obtained from inexpensive manganese present a rare case wherein excellent rate capability coexists with reversible oxygen redox activity. Our work shows the potential for designing cathode materials in the vast space between fully ordered and disordered compounds.

1 **Introduction**

2 The tremendous growth of lithium-based energy storage has put new emphasis on the discovery
3 of high energy density cathode materials¹. While state-of-the-art layered $\text{Li}(\text{Ni},\text{Mn},\text{Co})\text{O}_2$ (NMC)
4 cathodes achieve good power and energy density, potential further improvements on them are
5 limited. In addition, as the Li-ion industry grows to 1 TWh of production per year, approximately
6 1 million tons of combined cobalt or nickel will be required, putting significant strains on metal
7 resources². New cathodes with high energy density made from abundant metals are crucial to
8 sustain further Li-ion growth. Emerging materials, such as Li-rich layered oxides^{3,4} and cation-
9 disordered rocksalt-type cathodes (DRX)^{5,6}, despite showing record-high energy density, have
10 yet to demonstrate sufficient rate capability for fast rechargeable batteries, a limitation that has
11 been attributed to a large proportion of Li_2MnO_3 in the electrode formula⁴ or surface transition
12 metal (TM) densification upon O_2 loss^{7,8}.

13 When designing cathode materials, choosing a face-centered-cubic (FCC) anion framework is
14 most beneficial for achieving dense energy storage because it is a close-packed crystalline
15 arrangement. To obtain fast Li transport pathways and high power density, the cations, including
16 both Li and TM cations, should be optimally positioned within this anion framework. The
17 criterion for optimal cation arrangement is inspired by the recent discovery of the critical role of
18 inter-connecting low-energy migration channels in facilitating fast Li percolation⁹. A tetrahedral
19 site with no face-sharing TM ions (i.e. a 0-TM channel) exerts lower repulsion on a Li^+ ion that
20 passes through it than a tetrahedron that face-shares with one TM ion (i.e. a 1-TM channel),
21 which is particularly important when the structure is compact. It has been shown that a spinel-
22 like cation order (short-range or long-range) is most efficient at creating and percolating these 0-
23 TM channels (Figure 1a) through the structure at a lower Li/TM ratio than other common

ordering types¹⁰. This creates fast Li-ion networks, even in partially or fully disordered structures, and a high amount of kinetically accessible Li (Supplementary Note 1, Supplementary Figure 1 and Supplementary Table 1).

Conventional ordered spinel cathodes have been extensively investigated. LiMn_2O_4 can practically only be cycled between Mn_2O_4 and LiMn_2O_4 compositions¹¹, i.e. only over half the Li content per TM of layered analogues, providing about 480 Wh kg^{-1} . Ni substitution for Mn leads to a high-voltage spinel $\text{LiNi}_{0.5}\text{Mn}_{1.5}\text{O}_4$ with improved energy density, but both spinels have limited capacity as they cannot reliably cycle over the low-voltage plateau between LiM_2O_4 and $\text{Li}_2\text{M}_2\text{O}_4$ ^{12,13} (M = non-Li metal ions). A spinel with excess Li, $\text{Li}_4\text{Ti}_5\text{O}_{12}$ (16.7% M sites substituted by Li) shows desirable rate capability¹⁴, yet the low-voltage $\text{Ti}^{3+/4+}$ couple renders it unsuitable for cathode use¹⁵.

Here, in a departure from previous strategies, we design and demonstrate two bulk oxyfluorides with *partial* spinel-like order, $\text{Li}_{1.68}\text{Mn}_{1.6}\text{O}_{3.7}\text{F}_{0.3}$ and $\text{Li}_{1.68}\text{Mn}_{1.6}\text{O}_{3.4}\text{F}_{0.6}$ (referred to as LMOF03 and LMOF06 hereafter), achieving high energy density $>1,100 \text{ Wh kg}^{-1}$ and ultrafast rate capability. It should be noted that these compositions exhibit *cation over-stoichiometry* compared to the ideal LiM_2O_4 stoichiometry, i.e. their cation to anion ratio of 3.28:4 is larger than the 3:4 for ordered spinels, as well as *Li excess* since Li is partially substituted for Mn. The excess Li is used to increase the concentration of 0-TM channels for larger capacity and better Li transport kinetics, while the tunability in F substitution allows for lowered valences of Mn and improved cyclability¹⁶. Importantly, the unconventionally high Li-excess and fluorination levels are achieved through mutual facilitation: the excessive amount of Li is charge-balanced by F substitution, while the concentrated fluorination is only feasible because of the presence of the Li-rich local environments¹⁷. Finally, we use the cation over-stoichiometry to induce partial M

(dis)order so that the voltage step and first-order transition, characteristic of fully ordered spinels discharged past LiM_2O_4 composition, are removed. Remarkably, we find that half of the observed capacity in LMOF03 comes from reversible oxygen (O) redox, suggesting that the participation of anionic redox is not an intrinsic limitation to rate capability. Our results show the tremendous potential of designing high-performance and resource-efficient cathode materials in the large space between fully ordered compounds and random solid solutions.

Oxyfluorides with partial spinel-like order

LMOF03 and LMOF06 are synthesized through mechanochemical alloying. Elemental analysis shows their chemical compositions to be nearly identical to the targeted ones (Supplementary Table 2). We found that the over-stoichiometric Li is critical in stabilizing the high fluorination levels against phase segregation into LiF and Mn_2O_3 during synthesis. Structural refinements using combined synchrotron X-ray and neutron diffraction data confirm that both compounds adopt a spinel-like structure (space group: $Fd\bar{3}m$), with a pseudo FCC anion framework (outlined by dashed lines in Figure 1a). The site occupancies of Mn are obtained by refining X-ray diffraction patterns (Supplementary Figure 2), which are then taken as a starting model to fit the time-of-flight neutron data. Figure 1b shows the final neutron refinement, indicating good agreement between the observed and calculated peak positions and intensities (refinement details in Supplementary Tables 3–5 and Supplementary Figures 3 and 4). The refined lattice parameter is 8.1161(16) Å for LMOF03 and 8.1458(14) Å for LMOF06. In an ordered stoichiometric spinel, the tetrahedral 8a and octahedral 16d sites are fully occupied by Li and M, respectively, leaving the 8b and 16c sites vacant. In the two spinel-like oxyfluorides, however, complete cation order is not observed: (i) Mn is distributed between the 16c and 16d sites, with 14–16% of the total Mn

content occupying 16c sites; and (ii) only half of the 8a sites are occupied by Li. The remaining Li content is distributed between the 16c and 16d sites, with LMOF06 containing more Li in the 16c site than LMOF03. If we define a structure to be perfectly spinel-ordered (0% disorder) when all Mn is in the octahedral 16 site, or to be completely disordered (100% disorder) when Mn equally occupies the 16c and 16d sites, then the degree of disorder derived from the above structural refinement is 32.5% for LMOF03 and 27.5% for LMOF06.

The primary particle size is estimated using scanning electron microscopy (SEM) to be 100–200 nm for LMFO03 and 100–300 nm for LMOF06, as shown in Figures 1c and 1f. Agglomeration of primary particles into secondary particles is also observed (Supplementary Figure 5). The nano-scale crystalline lattice and elemental distribution are characterized using high-resolution transmission electron microscopy (HRTEM) and energy-dispersive spectroscopy (EDS). The results are shown in Figures 1d, 1e, 1g and 1h. For both materials, the size of the crystallite domains within the polycrystalline primary particles is estimated to be 10 nm. A characteristic *d*-spacing of ~ 4.8 Å for the spinel (111) faces is highlighted with white lines on crystallite grains that are properly orientated. Both materials show electron diffraction patterns that can be indexed based on a spinel crystal structure. ^7Li and ^{19}F solid-state nuclear magnetic resonance (NMR) spectroscopy suggests bulk integration of Li and F into the spinel structure (Supplementary Figures 6 and 7 and Supplementary Notes 2 and 3). Although LMOF06 might contain some diamagnetic impurities (Supplementary Note 2), the amount is unlikely to be significant because EDS elemental mapping across the particles reveal a uniform distribution of Mn, O and F (Figures 1e and 1h).

Large capacity beyond expected TM contribution

Both spinel-like ordered oxyfluorides demonstrate remarkable gravimetric capacity and energy density, as shown in Figures 2a and 2d. The theoretical Li capacity for both compounds is 2.4 Li per formula unit (f.u.) assuming all octahedral vacancies can be occupied, but with no face-sharing octahedral and tetrahedral occupancy (i.e., limiting compositions of $\text{Mn}_{1.6}\text{O}_{4-x}\text{F}_x$ and $\text{Li}_{2.4}\text{Mn}_{1.6}\text{O}_{4-x}\text{F}_x$ on charge and discharge, respectively), corresponding to 389 and 387 mA h g⁻¹ for LMOF03 and LMOF06, respectively. In the limiting Li composition of $\text{Li}_{2.4}\text{Mn}_{1.6}\text{O}_{4-x}\text{F}_x$, Mn is not expected to be fully reduced to Mn³⁺, making the theoretical Mn capacity based on the Mn^{3+/4+} redox couple 1.1 Li per f.u. (178 mA h g⁻¹) for LMOF03 and 1.4 Li per f.u. (226 mA h g⁻¹) for LMOF06. The Li site controlled discharge limit and the Mn⁴⁺ charge limit are marked in Figures 2b and 2e by vertical lines.

A capacity larger than the theoretical Mn redox capacity is observed for both compounds. When cycled at 50 mA g⁻¹ over the range 1.5–4.8 V, LMOF03 delivers a reversible capacity of 363 mA h g⁻¹ (a specific energy of 1,103 Wh kg⁻¹), corresponding to 2.25 Li per f.u., which is among the highest capacities reported to date for a Li-ion cathode^{5,6,18}. Even if discharge is limited to 2 V (or 3 V), the capacity and specific energy are still as high as 309 mA h g⁻¹ and 1,010 Wh kg⁻¹ (or 202 mA h g⁻¹ and 726 Wh kg⁻¹), respectively. Approximately half of the observed capacity in the 1.5–4.8 V range (~0.95 Li per f.u.) is obtained at Li contents below $x = 1.3$, when all Mn³⁺ is expected to be oxidized to Mn⁴⁺ (Figure 2b), suggesting the participation of a major charge compensation mechanism, possibly from oxygen, aside from the Mn redox. This extra capacity is accompanied by an increased voltage hysteresis. The maximum value of this hysteresis during the first cycle occurs near $x \sim 1.0$ and is approximately 0.91 V, which is comparable to that observed in heavily fluorinated disordered-rocksalts, e.g. $\text{Li}_2\text{Mn}_{2/3}\text{Nb}_{1/3}\text{O}_2\text{F}$ in 1.5–5 V and

Li₂MnO₂F in 2–4.8 V^{5,19}, but much smaller than that in Li-rich oxides, e.g. disordered-rocksalt Li_{1.3}Mn_{0.4}Nb_{0.3}O₂ (~1.45 V in 1.5–4.8 V)⁶ and layered Li_{1.2}Ni_{0.13}Mn_{0.54}Co_{0.13}O₂ (~1.23 V in 2.0–4.8 V)³. Such voltage hysteresis is commonly observed in Li-rich layered and disordered-rocksalt cathode materials that involve O redox and is likely associated with the different reaction paths between the charge and discharge processes, but the precise origin of it is not yet established. When narrowing the voltage window, hysteresis reduces and capacity retention improves. LMOF03 exhibits a slightly lower first-cycle gravimetric capacity (and energy) of 268 mA h g⁻¹ (868 W h kg⁻¹) when cycled between 2.0 and 4.6 V, and 218 mA h g⁻¹ (690 W h kg⁻¹) when cycled between 2.0 and 4.4 V. On the other hand, the doubled F content in LMOF06 increases the theoretical TM capacity to ~1.4 Li per f.u., resulting in improved cyclability and negligible concomitant oxygen loss (Supplementary Figures 8, 9 and 10). After 30 cycles, nearly 80% of the initial capacity is retained over the range 1.5–4.8 V, and ~93% is retained over the range 2.0–4.4 V. The voltage hysteresis is also noticeably smaller than for LMOF03, when comparing data collected over similar voltage windows.

The chemical and structural complexity of the spinel-like ordered oxyfluorides results in tunable voltage profiles. The two compounds show sloping voltage curves which provide easy monitoring of the state of charge, and which are different from the wide plateaus commonly observed in LiMn₂O₄ or LiNi_{0.5}Mn_{1.5}O₄¹², suggesting the suppression of two-phase reactions and stable Li-vacancy ordering. The observed capacity near 4 V is considerably lower than in LiMn₂O₄ due to the reduced Li occupancy in 8a sites. As a result of Li over-stoichiometry and partial cation (dis)order, a low number of Li⁺ in tetrahedral sites is energetically favored as it minimizes the interaction of Li⁺ with metal ions in adjacent face-sharing 16c sites. Consequently, more Li is active at a lower voltage of ~3 V, which is associated with the occupation of

octahedral sites. The voltage profile of LMOF06 is steeper than that of LMOF03, resulting in a slightly lower capacity of 305 mA h g^{-1} (931 Wh kg^{-1}) over the range 1.5–4.8 V. Given that the additional $\text{Mn}^{3+/4+}$ capacity in LMOF06 is unlikely to cause this difference, a plausible origin is that the larger F content in LMOF06 leads to a greater diversity of Li local environments and more F-bonded Li with higher site energy, thereby causing a steeper voltage. This speculation about the Li site distribution is also corroborated by the ^7Li NMR data, as the ^7Li pj-MATPASS spectrum obtained for LMOF06 is slightly broader than that for LMOF03 (Supplementary Figure 6).

1 **TM and anionic redox mechanisms**

2 To investigate the charge transfer mechanism that accompanies Li extraction and insertion,
3 operando X-ray absorption near-edge structure (XANES) in the hard X-ray region and *ex situ*
4 mapping of resonant inelastic X-ray scattering (mRIXS) measurements in the soft X-ray region
5 were performed.

6 The overall Mn redox behavior in LMOF03 is revealed by the Mn K-edge XANES spectra, as
7 shown in Figure 3a at selected states of charge. The material shows a reversible Mn redox
8 process, with no detectable Mn oxidation beyond 4+. In the initial charge, the Mn K-edge shifts
9 slightly to an energy close to that in MnO₂ (Mn⁴⁺ reference), consistent with the expected
10 contribution from the Mn^{3+/4+} redox capacity in this region. Upon discharge to 1.5 V, the edge
11 position reverses towards an energy between Mn₂O₃ (Mn³⁺ reference) and Mn₃O₄ (mixed
12 Mn²⁺/Mn³⁺), followed by reversible oxidation to Mn⁴⁺ again during the second charge. A similar
13 mechanism is observed for LMOF06 (Supplementary Figure 11), except that the pristine Mn
14 state is less oxidized (Supplementary Figure 15 and Supplementary Table 7) due to the higher F
15 content in the as-prepared material. Note that the main edges of the XANES spectra correspond
16 to the excitations of core electrons to Mn 4*p* states rather than the 3*d* valence states, and therefore
17 cannot be used to precisely quantify the Mn oxidation states²⁰.

18 To accurately quantify the Mn redox contribution as a function of the state of charge, we
19 employed Mn *L*-edge mRIXS on LMOF03 and extracted the inverse partial fluorescence yield
20 (iPFY) signal through a state-of-the-art high-efficiency mRIXS system^{21,22} (see technical details
21 on data analysis in Supplementary Figure 12). The extracted mRIXS-iPFY spectra at six
22 electrochemical states are displayed in Figure 3b (solid curves). The overall lineshape changes
23 slightly during the initial charge indicating limited Mn oxidation, but undergoes an obvious

1 evolution during the subsequent discharge, which when compared with the reference spectra
2 indicates a significant reduction of Mn. The observation is consistent with the trend of the hard
3 X-ray XANES results discussed above. As demonstrated in multiple previous cases, the Mn *L*-
4 edge spectral lineshape is sensitive to the Mn oxidation states and can be quantitatively fitted by
5 a linear combination of Mn^{2+/3+/4+} reference spectra²²⁻²⁴. The fitting results presented in Figure 3b
6 (dashed curves) agree with the experimental data (fitting details in Supplementary Table 6). The
7 Mn valence change and the amount of electron transfer due to Mn redox reactions thus obtained
8 are plotted in Figure 3d. The mRIXS-iPFY quantification of the Mn valence reveals that Mn
9 redox reactions mostly happen below 4.5 V on charge and between 3.6–1.5 V on discharge (grey
10 shaded areas). Above 4.5 V on charge, the Mn oxidation state slightly drops and remains largely
11 unchanged until 3.6 V discharged, indicating that the electrochemical capacity in this region (red
12 shaded area) is entirely contributed by a non-Mn redox processes.

13 A mismatch between cationic redox contribution and electrochemical capacity often indicates O
14 redox reactions; however, whether the activities are reversible remains unclear. We thus
15 employed a systematic study of O-*K* mRIXS. The technique reliably detects the oxidation of
16 lattice O by measuring the characteristic feature at around 523.7 eV emission energy and 531.0
17 eV excitation energy^{22,25,26} (orange arrows in Figure 3c), which originates from an excitation to
18 unoccupied/oxidized O 2*p* orbitals²⁶. This characteristic signal emerges at 4.5 V and grows
19 stronger in intensity upon the charge to 4.8 V, and reversibly weakens during discharge until 2.7
20 V. The reversible evolution of the mRIXS feature upon cycling provides direct experimental
21 evidence for reversible lattice O redox processes in our electrode system.

22 The combined Mn-*L* and O-*K* mRIXS results consistently reveal the Mn and O redox mechanism:
23 the contribution of Mn redox reactions to electrochemical capacity (grey shade in Figure 3d) is

1 limited during the initial charge but becomes more dominant during discharge below 3.6 V. On
2 the other hand, O oxidation (red shade in Figure 3d) dominates the charge process, followed by
3 reversible lattice O reduction until 2.7 V. Note that the mRIXS observation of extended anionic
4 redox activity towards low voltages during discharge has been found in many other Li-ion and
5 Na-ion electrodes^{22,27}. In addition, the slight drop in Mn valence state when charged from 4.5 V
6 to 4.8 V strongly indicates the impact of TM-O coupling nature on O oxidation processes, a
7 phenomenon that was noted before^{28,29}.

8 During the second charge, as shown in Supplementary Figures 13, 14 and Supplementary Table
9 6, the observed capacity initially originates from Mn oxidation when the voltage is below 2.95 V.
10 It then shows mixed contribution from both Mn and O oxidation until 4.0 V, above which the
11 Mn oxidation state remains nearly constant, leaving O oxidation as the only source for electron
12 extraction. After the following discharge, the Mn valence reversibly decreases to a value close to
13 that observed after the first full cycle.

14 The reversible redox reactions are consistent with a reversible lattice change during cycling as
15 shown in the *ex-situ* X-ray diffraction patterns (Supplementary Figure 16). The data reveal a
16 similar trend for LMOF03 and LMOF06, with the second-cycle charge process restoring the
17 same delithiated lattice as after the first charge. *Ex-situ* synchrotron diffraction (Supplementary
18 Note 4, Supplementary Figures 17 and 18) confirms the preservation of a spinel structure during
19 cycling. The extent of Mn disorder in the 16d and 16c octahedral sites as obtained by Rietveld
20 refinement remains constant upon charge and only increases when discharged below 2.7 V,
21 which then gets reversed during the subsequent charge process.

22

1 **Ultrahigh rate capability despite O redox**

2 Ultrahigh rate capability is observed in LMOF03 and LMOF06, as shown in Figures 4a–4d. All
3 rate capability tests are carried out using galvanostatic charge and discharge at the specified rate
4 without holding the voltage at the top of charge. At the extremely high rates from 4 to 20 A g⁻¹,
5 to remove all other possible rate limitations, we dilute the electrode and increase its electron
6 conductivity by using high carbon loading. A material for similarly high rate capability was
7 initially established in high carbon content electrodes³⁰. While this shows the intrinsic rate
8 capability of the cathode material, in commercial electrodes, the carbon loading would have to be
9 reduced through carbon coating to more efficiently form a conductive network, as has been
10 demonstrated for LiFePO₄³¹.

11 At 100 mA g⁻¹, LMOF03 delivers a gravimetric capacity of over 370 mA h g⁻¹. When cycled 20
12 times faster at 2,000 mA g⁻¹, the observed capacity is reduced only moderately by ~30% to 260
13 mA h g⁻¹ and the discharge process takes ~8 minutes. Since the theoretical Mn capacity is only
14 178 mA h g⁻¹ in LMOF03, a significant portion of the observed capacity at 2,000 mA g⁻¹ is still
15 expected to originate from reversible O redox. The fact that such large capacities are able to
16 sustain high rates of charge and discharge despite a major contribution from O redox is in
17 contrast to previous observations of sluggish kinetics in O-redox-involved Li-rich layered oxide
18 cathodes^{32,33} or cation-disordered rocksalts^{5,6}. Our observation suggests that O redox is not
19 intrinsically slow. Instead, it is possible that the specific local environments that stabilize
20 oxidized O species are sluggish in their formation in other compounds, e.g., because their
21 formation may involve slow M migration. M migration has been often observed at high voltages
22 accompanying O redox in Li-rich layered cathodes³⁴. In contrast, in our materials, no significant
23 increase in M disorder is observed even at the top of charge (Supplementary Figures 17 and 18).

Hence, it is possible that the ultrafast kinetics in LMOF03 even with major O redox contributions is due to the lack of metal migration. But further investigation is required to provide a detailed mechanism. LMOF06 exhibits an even higher rate capability than LMOF03, with less pronounced polarization growth as the rate increases from 100 mA g⁻¹ to 20 A g⁻¹.

The rate performance of the two spinel-like oxyfluorides is compared to state-of-the-art Li-ion cathodes in a Ragone plot shown in Figure 4e. Only the best rate capability reported in literature, achieved through nano-sizing, surface coating or discharge after slow charging or voltage-holding, is included^{5,19,32,35-37} (details in Supplementary Table 8). When compared to cathodes that involve O redox as part of their charge compensation mechanism, e.g. Li_{1.2}Mn_{0.4}Ti_{0.4}O₂, Li₂Mn_{2/3}Nb_{1/3}O₂F and Li-rich NMC, the specific power of LMOF03 and LMOF06 at any given energy density is at least one order of magnitude higher, resulting in the delivery of, e.g., 900 Wh kg⁻¹ of energy, within minutes rather than hours. Even when compared to the state-of-the-art LiNi_{0.8}Mn_{0.1}Co_{0.1}O₂ cathode, at the highest literature-reported specific power ~3,000 W kg⁻¹, both LMOF03 and LMOF06 are still superior in terms of specific energy.

The importance of cation over-stoichiometry and Li excess

Fully ordered structures are discrete endpoints of the extensive configurational space of partially (dis)ordered materials. Relaxing the requirement for long-range order in cathode materials enables one to access new degrees of freedom to design their electrochemical properties but requires a precise understanding of the role that each chemical and structural variable plays in the materials performance.

The two partially ordered oxyfluoride spinels shown in this paper are representatives of our strategy to use partial cation order to simultaneously tune multiple chemical and structural factors, as shown in the illustration in Figure 5. We chose to start from a spinel endpoint with the knowledge that spinel-type cation short-range order creates a robust percolation of low-barrier Li migration channels that persists even at fairly low Li/M ratio¹⁰. The cation over-stoichiometry and partial order introduces extra Li and creates partial occupancy on 16c sites, while reducing the occupancy on 8a and 16d sites, thereby creating a state that is in between an ordered spinel and a disordered rocksalt. This state of partial order enables several compositional and structural modifications that are beneficial to performance.

The cation/Li over-stoichiometry facilitates partial M (dis)order by reducing tetrahedral occupancy and thus relaxing the constraint that M ions must order in a *facial* configuration on all octahedral cation clusters, leading to the diverse cation arrangements shown in Figure 5a. This partial (dis)order removes the collective 8a-to-16c Li migration which in ordered spinels is responsible for a first-order phase transition and a large voltage step when they are lithiated past the LiM_2O_4 composition. As Figure 2 shows, in the partially ordered LMOF03 and LMOF06, the voltage profiles show no discernible steps or phase transitions, leading to more facile charge and discharge.

1 A key factor in the high rate capability is likely the cation-over-stoichiometry and the resulting
2 partial M order. Additional cations cannot be inserted to a spinel during an electrochemical
3 process without creating face-sharing polyhedra of tetrahedral and octahedral cations. While M-
4 Li or M-M face sharing is highly unlikely due to their strong electrostatic repulsion, Li-Li face
5 sharing may be possible at least in metastable configurations. Very high Li mobility in anodes³⁸
6 and solid state electrolytes³⁹ has recently been linked to such Li-Li face sharing as it creates
7 configurational frustration and high-energy Li states that are beneficial to Li mobility.

8 Besides enhancing transport and percolation, Li excess (i.e., Li substitution) also activates O
9 redox and enables partial substitution of O by F, which is important to lower the Mn valence and
10 has in other materials been shown to reduce or remove O loss when anion redox is present⁵. The
11 manner by which Li excess enables anion redox and fluorination in these materials can be
12 understood from the local anion bonding environment, as illustrated in Figure 5b. In a
13 conventional stoichiometric spinel LiMn_2O_4 , each anion is covalently bonded to three Mn ions.
14 When Li excess is introduced, the number of Li-rich local environments increases, thereby
15 enabling easier fluorination with fewer high-energy Mn-F bonds for each F^- ion substituted¹⁷.
16 The increased number of ionic O-Li bonds also leads to the appearance of high-lying
17 unhybridized O $2p$ orbitals acting as reservoir of additional oxidizable electrons⁴⁰.

18 In summary, two design guidelines are followed in this work. First, Li over-stoichiometry, i.e.,
19 shifting the composition from LiMn_2O_4 to $\text{Li}_{1.28}\text{Mn}_2\text{O}_4$, is utilized to induce partial Mn disorder,
20 thereby eliminating the first-order transition and obtaining a smooth and continuous voltage
21 profile without discrete steps. Second, Li excess, i.e., shifting the composition further from
22 $\text{Li}_{1.28}\text{Mn}_2\text{O}_4$ to $\text{Li}_{1.68}\text{Mn}_{1.6}(\text{O},\text{F})_4$, is introduced to increase the kinetically accessible Li capacity
23 and to enable fluorination and reversible O redox with more Li-rich environments. The two

1 cathode materials thus obtained, LMOF03 and LMOF06, exhibit capacities and rate capabilities
2 among the highest reported to date. Our simple yet effective design strategy, which combines a
3 partially ordered spinel-like structure with substantial Li excess and fluorination, opens up a vast
4 chemical space for the search of new cathodes with both high energy and power, and made from
5 earth-abundant metals. Future improvement are expected in these materials through partial
6 replacement of Mn^{4+} by high-valence non-redox-active d^{10} or d^0 ions (e.g. Sb^{5+} , Nb^{5+} and Mo^{6+}),
7 and through the exploration of different or mixed redox-active TM species (e.g. Ni^{2+} , V^{3+} , Cr^{3+}),
8 as well as through fine tuning of the fluorination level to allow for an optimized balance between
9 TM and O redox. The insight gained about partial structural order tuning in relation with
10 electrochemical performance is also applicable to the materials design of Li-ion anodes as well
11 as the optimization of conductivity in solid-state electrolytes for beyond Li-ion technologies.

12

Conclusions

We have demonstrated that combining kinetically advantageous partial spinel-like cation order with substantial Li excess and F substitution is effective for achieving both high energy density and excellent rate capability in Li-ion battery cathodes. Following these design strategies, high specific energy $>1,100 \text{ Wh kg}^{-1}$ (and capacity $>360 \text{ mA h g}^{-1}$) is obtained for $\text{Li}_{1.68}\text{Mn}_{1.6}\text{O}_{3.7}\text{F}_{0.3}$, with nearly half of the capacity coming from O redox processes, a phenomenon that has been intensely studied in Li-rich layered Ni-Mn-Co oxides and disordered rocksalts but is uncommon in spinel-type cathodes. A significant proportion of the capacity is retained at high cycling rates. Furthermore, we showed that the two chemical handles for structural tuning, namely cation overstoichiometry and Li excess, can be strategically optimized to allow for fast Li transport kinetics, optimized voltage profiles, and a largely tunable F doping level and thus TM capacity to achieve the desired cyclability. Our discovery provides a paradigm for the realization of both fast and dense energy storage in Li-ion cathode materials.

1 **Methods**

2 **Synthesis.** $\text{Li}_{1.68}\text{Mn}_{1.6}\text{O}_{3.7}\text{F}_{0.3}$ and $\text{Li}_{1.68}\text{Mn}_{1.6}\text{O}_{3.4}\text{F}_{0.6}$ were synthesized by mixing stoichiometric
3 Li_2MnO_3 (obtained by firing Li_2CO_3 (Alfa Aesar, 99.0%) and MnO_2 (Alfa Aesar, 99.9%) at 800
4 °C in air for 16 hours), MnF_2 (Alfa Aesar, 99%), Mn_2O_3 (sigma-Aldrich, 99%) and MnO_2 using a
5 Retsch PM200 planetary ball mill. Precursor powder of a batch size of 1 g, along with five 10-
6 mm (diameter) and ten 5-mm (diameter) stainless-steel balls, was dispensed into a 50-ml
7 stainless-steel jar, which was then sealed with safety closure clamps in an argon-filled glovebox.
8 We monitored the purity of products by performing ex-situ X-ray diffraction after every 5 or 10
9 hours of mechanochemical ball milling and adjusted the synthesis time accordingly. After high-
10 energy ball-milling at 450 rpm for 25 and 21 hours, for $\text{Li}_{1.68}\text{Mn}_{1.6}\text{O}_{3.7}\text{F}_{0.3}$ and $\text{Li}_{1.68}\text{Mn}_{1.6}\text{O}_{3.4}\text{F}_{0.6}$,
11 respectively, the phase-pure product was obtained mechanochemically. The two target materials
12 can also be obtained using a different set of precursors, including Li_2O , Mn_2O_3 , MnO_2 and LiF .
13 Note that we present $\text{Li}_{1.68}\text{Mn}_{1.6}\text{O}_{3.4}\text{F}_{0.6}$ as the composition with the highest fluorination in
14 manuscript because this is the limit at which we are confident about the solubility of F. Above
15 this level, impurities LiF and Mn_2O_3 as determined by XRD show up. We also synthesized
16 LiMn_2O_4 as a baseline material by ball milling a stoichiometric mixture of Li_2MnO_3 , Mn_2O_3 , and
17 MnO_2 , under the same conditions as for LMOF03 and LMOF06. After 12 hours of milling, an X-
18 ray diffraction pattern indexed to a phase-pure LiMn_2O_4 without impurity peaks was obtained
19 (Supplementary Figure 19a and Supplementary Note 5).

20 **Electrochemistry.** The fabrication of cathode electrodes was done in an argon-filled glovebox.
21 The active material (70 wt%) was first manually mixed with Super C65 carbon black (Timcal, 20
22 wt%) in a mortar for 45 minutes. After adding polytetrafluoroethylene (PTFE, Dupont, 10 wt%)
23 as a binder, the mixture was rolled into a thin film to be used as a cathode. The loading density of

the cathode film is $\sim 5 \text{ mg cm}^{-2}$. Coin cells (CR2032) were assembled by using 1 M LiPF_6 in ethylene carbonate and dimethyl carbonate solution (volumetric 1:1, Sigma-Aldrich, battery grade) as the electrolyte, glass microfiber filters (Whatman) as separators, and Li metal foil (FMC) as the anode. The sealed coin cells were then tested on an Arbin battery cycler at room temperature. For rate capability tests at high current densities from 4 to 20 A g^{-1} , the weight ratio of active material, carbon black and binder in cathode films was 4:5:1 and the loading density of the cathode film is $2\text{--}3 \text{ mg cm}^{-2}$.

Compositional, structural and morphological characterization. Elemental analysis was performed by Luvak Inc using direct-current plasma emission spectroscopy (ASTM E 1097-12) for metal species and an ion selective electrode method (ASTM D1179-16) for fluorine. Ex-situ synchrotron diffraction of both pristine and cycled powder was taken at the Advanced Photon Source in Argonne National Laboratory (ANL) on Beamline 11-ID-B ($\lambda = 0.2113 \text{ \AA}$). The cycled powder was prepared by mixing pristine material with carbon (in a 9:1 weight ratio), cycling the loose powder mixture at 5 mA g^{-1} , followed by equilibrating at the designated voltage until the current was below 0.2 mA g^{-1} . The obtained powder was then washed with dimethyl carbonate and dried in vacuum. Neutron powder diffraction experiment was carried out at the Spallation Neutron Source in Oak Ridge National Laboratory on the Nanoscale Ordered Materials Diffractometer (NOMAD)⁴¹. The samples for neutron diffraction were synthesized using a ^7Li -enriched precursor $^7\text{Li}_2\text{MnO}_3$, which was obtained by calcinating stoichiometric $^7\text{Li}_2\text{CO}_3$ and MnO_2 at 800°C in air for 16 hours. All the synchrotron and neutron data were analyzed using the TOPAS software package.⁴² Scanning transmission electron microscopy, electron diffraction patterns and EDS mapping were acquired at the Molecular Foundry in Lawrence Berkeley National Laboratory on a JEM-2010F microscope equipped with an X-mas EDS detector. SEM

images were also obtained at the Molecular Foundry on a Zeiss Gemini Ultra 55 analytical field-emission scanning electron microscope.

Operando Mn K-edge X-ray absorption spectroscopy. For the operando X-ray absorption near-edge structure (XANES) experiments, modified coin cells were used with holes in the center of all stainless-steel parts and sealed with X-ray transparent Kapton tapes. A galvanostatic scan rate of 30 mA g⁻¹ was used. The measurement was conducted in transmission mode at room temperature using Beamline 20-BM at the Advanced Photon Source (APS) of Argonne National Laboratory (ANL). The incident energy was selected using a Si (111) monochromator and the beam intensity was reduced by 15 % using a Rh-coated mirror to minimize high-order harmonics. Reference spectra of Mn metal were collected simultaneously using a pure Mn foil. The resultant XANES data were analyzed using the Athena software package. The energies of spectra were calibrated using the first inflection points from the reference Mn spectrum.

Mapping of resonant inelastic X-ray scattering (mRIXS). mRIXS was measured at the iRIXS endstation on Beamline 8.0.1 of the Advanced Light Source in Lawrence Berkeley National Laboratory²¹. The mapping data were collected using an ultra-high efficiency modular spectrometer⁴³ with an excitation energy step of 0.2 eV. The resolution of the excitation energy was 0.35 eV and that of the emission energy was 0.25 eV. The final 2D maps were obtained via multi-step data processing as elaborated in a previous study⁴⁴. The intensity of the mRIXS is represented by a color scale.

Mn-*L*₃ inverse partial fluorescence yield (iPFY). Mn-*L*₃ iPFY was achieved through the formula $iPFY = a/PFY_O$, where a is a normalization coefficient and PFY_O is the integrated fluorescence intensity over the O-*K* emission energy range (490 to 530 eV, white dashed box in Supplementary Figure 12a) from the Mn-*L*₃ mRIXS. In contrast to the distorted total

fluorescence yield obtained from conventional Mn- L_3 soft X-ray absorption spectroscopy (sXAS-TFY, shown as a yellow solid spectrum in Supplementary Figure 12b), the non-distorted Mn- L_3 iPFY spectra can be quantitatively fitted using a linear combination of the standard spectra of Mn^{2+/3+/4+}, as demonstrated and detailed before²³.

Solid-state nuclear magnetic resonance spectroscopy (ssNMR). ¹⁹F and ⁷Li NMR data were collected on both LMOF03 and LMOF06 powders using a Bruker Avance 300 MHz (7.05 T) wide-bore NMR spectrometer with Larmor frequencies of 282.40 MHz and 116.64 MHz, respectively, at room temperature. The data was obtained using 60 kHz magic-angle spinning (MAS) with a 1.3 mm double-resonance probe. ¹⁹F and ⁷Li NMR data were referenced to LiF ($\delta(^{19}\text{F}) = -204$ ppm and $\delta(^7\text{Li}) = -1$ ppm). Lineshape analysis was carried out within the Bruker Topspin software using the SOLA lineshape simulation package.

⁷Li spin echo spectra were acquired on all samples using a 90° radiofrequency (RF) pulse of 0.6 μ s and a 180° RF pulse of 1.2 μ s at 200 W. A recycle delay of 30 s was used for LiF while a recycle delay of 50 ms was used for LMOF03 and LMOF06. ⁷Li pj-MATPASS (projected Magic-Angle Turning Phase-Adjusted Sideband Separation)⁴⁵ isotropic spectra were also acquired on the LMOF03 and LMOF06 samples using a 90° RF pulse of 0.6 μ s at 200 W with a recycle delay of 50 ms.

The resonant frequency range of the ¹⁹F nuclei in the LMOF03 and LMOF06 samples was larger than the excitation bandwidth of the RF pulse used in the NMR experiment. To obtain the full spectrum, nine spin echo spectra were collected for each sample in frequency steps of 280 ppm or 79 kHz from -1120 to 1120 ppm, where the step size was slightly less than the excitation bandwidth of the RF pulse. The individual sub-spectra were processed using a zero-order phase correction and then added to give an overall sum spectrum in the absorption mode that required

no further phase correction. This method, termed “spin echo mapping”⁴⁶, “frequency stepping”^{47,48}, or “VOCS” (Variable Offset Cumulative Spectrum)⁴⁹, is able to uniformly excite the broad F signals by providing a large excitation bandwidth. Individual ¹⁹F spin echo spectra were collected using a 90° RF pulse of 2.9 μs and a 180° RF pulse of 5.8 μs at 154.8 W with a recycle delay of 50 ms. For reference, a spin echo spectrum was collected for LiF using similar RF pulses but with a recycle delay of 30 s. A ¹⁹F background spectrum obtained on the empty probe using the same conditions as the LMOF03 and LMOF06 samples showed no significant background signal.

Differential electrochemical mass spectrometer (DEMS) measurement. Gas evolution measurements were collected using a differential electrochemical mass spectrometer (DEMS) system as described in previous publications^{16,50}. Electrochemical cells of modified Swagelok design were prepared in a glovebox with thin film cathodes composed of active materials (70 wt%), Super C65 carbon black (Timcal, 20 wt%), and PTFE (Dupont, 10 wt%) and a loading density of ~7mg cm⁻² (based on active materials). The electrolyte, separators, and anodes used were identical to those used for the coin cell tests in this study. DEMS cells were cycled with a current density of 20 mA g⁻¹ under a static head of argon pressure (~0.2 bar) at room temperature.

Li percolation simulations. Percolating Li diffusion pathways through 0-TM channels were computed using the Monte Carlo method of reference 10 as implemented in the Dribble software (<https://github.com/urban-group/dribble>). All simulations employed cubic cells with 3,456 Li_xTM_yO₂ formula units (6,912 cation sites) that are commensurate with the layered (α-NaCoO₂), spinel (Li₂Mn₂O₄), γ-LiFeO₂, and rocksalt crystal structures. Each simulation was repeated 500 times. Percolation of 0-TM diffusion pathways and kinetically accessible 0-TM capacities in the ideal cation orderings of spinel and the layered structure was determined by decorating all cation

1 sites with TM ions at the beginning of the simulation, followed by substituting Li for TM on a
2 randomly selected site of the Li sublattice at each Monte Carlo step. Once the Li sublattice was
3 fully decorated with Li ions, the Li substitution was continued for the sites of the TM sublattice.
4 Cation mixing was modeled by interchanging a fraction of the sites on the Li and TM sublattices
5 at the beginning of the simulation. Interchanging 50% of the sites results in equivalence of the
6 two sublattices and corresponds to the fully disordered rocksalt structure (i.e., the degree of
7 cation mixing is 100%). More details can be found in reference 10.

9 **Acknowledgement**

10 This work is supported by the Umicore Specialty Oxides and Chemicals and the Assistant
11 Secretary of Energy Efficiency and Renewable Energy, Vehicle Technologies Office of the U.S.
12 Department of Energy (DOE) under Contract No. DE-AC02-05CH11231 under the Advanced
13 Battery Materials Research (BMR) Program. Work at the Advanced Light Source is supported
14 by the Director, Office of Science, Office of Basic Energy Sciences, of the U.S. DOE under
15 Contract No. DE-AC02-05CH11231. Research conducted at the NOMAD Beamline at Oak
16 Ridge National Laboratory's Spallation Neutron Source is sponsored by the Scientific User
17 Facilities Division, Office of Basic Sciences of the U.S. DOE. Work at the Molecular Foundry at
18 Lawrence Berkeley National Laboratory is supported by the Office of Science, Office of Basic
19 Energy Sciences of the U.S. DOE under Contract No. DE-AC02-05CH11231. This research used
20 resources of the Advanced Photon Source, an Office of Science User Facility operated for the
21 U.S. DOE Office of Science by Argonne National Laboratory, and is supported by the U.S. DOE
22 under Contract No. DE-AC02-06CH11357. The NMR experimental work reported here made

1 use of the shared facilities of the UCSB MRSEC (NSF DMR 1720256), a member of the
2 Material Research Facilities Network. J.K.P. also acknowledges support from the NSF Graduate
3 Research Fellowship under contract No. DGE-1106400.

4

5

6

1 **Data availability**

- 2 The datasets generated and analyzed during the current study are available from the
- 3 corresponding author on reasonable request.

Author contributions

H.J. and G.C. planned the project. G.C. supervised all aspects of the research. H.J. designed the proposed compounds. H.J. and Z.C. synthesized and electrochemically tested the compounds with help from H.K. J.W. performed mRIXS measurements and analyzed the data with input from W.Y. J.L. performed neutron diffraction measurement and analyzed the neutron and synchrotron diffraction data. D.-H.K. acquired and analyzed TEM, ED and EDS data. H.K. collected operando XANES data with help from M.B. and Z.C. A.U. performed computational percolation analysis. J.K.P. acquired and analyzed DEMS data with input from B.D.M. E.F. acquired and analyzed NMR data with input from R.J.C. Y.T. collected SEM and synchrotron diffraction data. The manuscript was written by H.J. and G.C. and was revised by A.U., J.W. and J.L. with the help from other authors.

1 References

- 2 1 Xu, B., Qian, D., Wang, Z. & Meng, Y.S. Recent progress in cathode materials research for
3 advanced lithium ion batteries. *Mat. Sci. Eng. R.* **73**, 51–65 (2012).
- 4 2 Olivetti, E.A., Ceder, G., Gaustad, G.G. & Fu, X. Lithium-ion battery supply chain considerations:
5 analysis of potential bottlenecks in critical metals. *Joule* **1**, 229–243 (2017).
- 6 3 Thackeray, M.M. *et al.* Li₂MnO₃-stabilized LiMO₂ (M= Mn, Ni, Co) electrodes for lithium-ion
7 batteries. *J. Mater. Chem.* **17**, 3112–3125 (2007).
- 8 4 Yu, X. *et al.* Understanding the Rate Capability of High-Energy-Density Li-Rich Layered
9 Li_{1.2}Ni_{0.15}Co_{0.1}Mn_{0.55}O₂ Cathode Materials. *Adv. Energy Mater.* **4**, 1300950 (2014).
- 10 5 Lee, J. *et al.* Reversible Mn²⁺/Mn⁴⁺ double redox in lithium-excess cathode materials. *Nature* **556**,
11 185–190 (2018).
- 12 6 Yabuuchi, N. *et al.* High-capacity electrode materials for rechargeable lithium batteries: Li₃NbO₄-
13 based system with cation-disordered rocksalt structure. *Proc. Natl Acad. Sci. USA* **112**, 7650–
14 7655 (2015).
- 15 7 Lee, J. *et al.* A new class of high capacity cation-disordered oxides for rechargeable lithium
16 batteries: Li–Ni–Ti–Mo oxides. *Energy Environ. Sci.* **8**, 3255–3265 (2015).
- 17 8 Armstrong, A.R. *et al.* Demonstrating oxygen loss and associated structural reorganization in the
18 lithium battery cathode Li[Ni_{0.2}Li_{0.2}Mn_{0.6}]O₂. *J. Am. Chem. Soc.* **128**, 8694–8698 (2006).
- 19 9 Lee, J. *et al.* Unlocking the potential of cation-disordered oxides for rechargeable lithium
20 batteries. *Science* **343**, 519–522 (2014).
- 21 10 Urban, A., Lee, J. & Ceder, G. The Configurational Space of Rocksalt-Type Oxides for High-
22 Capacity Lithium Battery Electrodes. *Adv. Energy Mater.* **4**, 1400478 (2014).
- 23 11 Gummow, R., De Kock, A. & Thackeray, M. Improved capacity retention in rechargeable 4 V
24 lithium/lithium-manganese oxide (spinel) cells. *Solid State Ionics* **69**, 59–67 (1994).
- 25 12 Manthiram, A., Chemelewski, K. & Lee, E.-S. A perspective on the high-voltage LiMn_{1.5}Ni_{0.5}O₄
26 spinel cathode for lithium-ion batteries. *Energy Environ. Sci.* **7**, 1339–1350 (2014).
- 27 13 Lee, E.-S., Nam, K.-W., Hu, E. & Manthiram, A. Influence of cation ordering and lattice
28 distortion on the charge–discharge behavior of LiMn_{1.5}Ni_{0.5}O₄ spinel between 5.0 and 2.0 V.
29 *Chem. Mater.* **24**, 3610–3620 (2012).
- 30 14 Feckl, J.M. *et al.* Nanoscale porous framework of lithium titanate for ultrafast lithium insertion.
31 *Angew. Chem. Int. Ed.* **51**, 7459–7463 (2012).
- 32 15 Ferg, E., Gummow, R., De Kock, A. & Thackeray, M. Spinel anodes for lithium-ion batteries. *J.*
33 *Electrochem. Soc.* **141**, L147–L150 (1994).

- 16 Lee, J. *et al.* Mitigating oxygen loss to improve the cycling performance of high capacity cation-disordered cathode materials. *Nat. Commun.* **8**, 981 (2017).
- 17 Richards, W.D., Dacek, S.T., Kitchaev, D.A. & Ceder, G. Fluorination of Lithium-Excess Transition Metal Oxide Cathode Materials. *Adv. Energy Mater.* **8**, 1701533 (2018).
- 18 Zuo, Y. *et al.* A High-Capacity O2-Type Li-Rich Cathode Material with a Single-Layer Li₂MnO₃ Superstructure. *Adv. Mater.* **30**, 1707255 (2018).
- 19 House, R.A. *et al.* Lithium manganese oxyfluoride as a new cathode material exhibiting oxygen redox. *Energy Environ. Sci.* **11**, 926–932 (2018).
- 20 Manceau, A., Marcus, M.A. & Grangeon, S. Determination of Mn valence states in mixed-valent manganates by XANES spectroscopy. *Am. Mineral.* **97**, 816–827 (2012).
- 21 Qiao, R. *et al.* High-efficiency in situ resonant inelastic x-ray scattering (iRIXS) endstation at the Advanced Light Source. *Rev. Sci. Instrum.* **88**, 033106 (2017).
- 22 Dai, K. *et al.* High Reversibility of Lattice Oxygen Redox Quantified by Direct Bulk Probes of Both Anionic and Cationic Redox Reactions. *Joule* **3**, 518–541 (2019).
- 23 Li, Q. *et al.* Quantitative probe of the transition metal redox in battery electrodes through soft x-ray absorption spectroscopy. *J. Phys. D: Appl. Phys.* **49**, 413003 (2016).
- 24 Qiao, R. *et al.* Revealing and suppressing surface Mn (II) formation of Na_{0.44}MnO₂ electrodes for Na-ion batteries. *Nano Energy* **16**, 186–195 (2015).
- 25 Yang, W. & Devereaux, T.P. Anionic and cationic redox and interfaces in batteries: Advances from soft X-ray absorption spectroscopy to resonant inelastic scattering. *J. Power Sources* **389**, 188–197 (2018).
- 26 Zhuo, Z. *et al.* Spectroscopic signature of oxidized oxygen states in peroxides. *J. Phys. Chem. Lett.* **9**, 6378–6384 (2018).
- 27 Gent, W.E. *et al.* Coupling between oxygen redox and cation migration explains unusual electrochemistry in lithium-rich layered oxides. *Nat. Commun.* **8**, 2091 (2017).
- 28 Sathiya, M. *et al.* Reversible anionic redox chemistry in high-capacity layered-oxide electrodes. *Nat. Mater.* **12**, 827–835 (2013).
- 29 Luo, K. *et al.* Anion redox chemistry in the cobalt free 3d transition metal oxide intercalation electrode Li[Li_{0.2}Ni_{0.2}Mn_{0.6}]O₂. *J. Am. Chem. Soc.* **138**, 11211–11218 (2016).
- 30 Kang, B. & Ceder, G. Battery materials for ultrafast charging and discharging. *Nature* **458**, 190–193 (2009).
- 31 Dominko, R. *et al.* Impact of the carbon coating thickness on the electrochemical performance of LiFePO₄/C composites. *J. Electrochem. Soc.* **152**, A607–A610 (2005).

- 32 Martha, S.K., Nanda, J., Veith, G.M. & Dudney, N.J. Electrochemical and rate performance study of high-voltage lithium-rich composition: $\text{Li}_{1.2}\text{Mn}_{0.525}\text{Ni}_{0.175}\text{Co}_{0.1}\text{O}_2$. *J. Power Sources* **199**, 220–226 (2012).
- 33 Konishi, H., Gunji, A., Feng, X. & Furutsuki, S. Effect of transition metal composition on electrochemical performance of nickel-manganese-based lithium-rich layer-structured cathode materials in lithium-ion batteries. *J. Solid State Chem.* **249**, 80–86 (2017).
- 34 Hong, J. *et al.* Metal–oxygen decoordination stabilizes anion redox in Li-rich oxides. *Nat. Mater.* **18**, 256–265 (2019).
- 35 Teranishi, T. *et al.* High-rate capabilities of ferroelectric BaTiO_3 – LiCoO_2 composites with optimized BaTiO_3 loading for Li-ion batteries. *ECS Electrochem. Lett.* **4**, A137–A140 (2015).
- 36 Ji, H. *et al.* Hidden structural and chemical order controls lithium transport in cation-disordered oxides for rechargeable batteries. *Nat. Commun.* **10**, 592 (2019).
- 37 Noh, H.-J., Youn, S., Yoon, C.S. & Sun, Y.-K. Comparison of the structural and electrochemical properties of layered $\text{Li}[\text{Ni}_x\text{Co}_y\text{Mn}_z]\text{O}_2$ ($x = 1/3, 0.5, 0.6, 0.7, 0.8$ and 0.85) cathode material for lithium-ion batteries. *J. Power Sources* **233**, 121–130 (2013).
- 38 Schmidt, W. *et al.* Small Change-Great Effect: Steep Increase of Li Ion Dynamics in $\text{Li}_4\text{Ti}_5\text{O}_{12}$ at the Early Stages of Chemical Li Insertion. *Chem. Mater.* **27**, 1740–1750 (2015).
- 39 Kozinsky, B. *et al.* Effects of sublattice symmetry and frustration on ionic transport in garnet solid electrolytes. *Phys. Rev. Lett.* **116**, 055901 (2016).
- 40 Seo, D.-H. *et al.* The structural and chemical origin of the oxygen redox activity in layered and cation-disordered Li-excess cathode materials. *Nat. Chem.* **8**, 692–697 (2016).
- 41 Neuefeind, J. *et al.* The nanoscale ordered materials diffractometer NOMAD at the spallation neutron source SNS. *Nucl. Instrum. Meth. Phys. Res. B* **287**, 68–75 (2012).
- 42 Coelho, A.A. TOPAS and TOPAS-Academic: an optimization program integrating computer algebra and crystallographic objects written in C++. *J. Appl. Crystallogr.* **51**, 210–218 (2018).
- 43 Chuang, Y.-D. *et al.* Modular soft x-ray spectrometer for applications in energy sciences and quantum materials. *Rev. Sci. Instrum.* **88**, 013110 (2017).
- 44 Wu, J. *et al.* Elemental-sensitive detection of the chemistry in batteries through soft x-ray absorption spectroscopy and resonant inelastic x-ray scattering. *J. Vis. Exp.* **134**, e57415 (2018).
- 45 Hung, I. *et al.* Isotropic high field NMR spectra of Li-ion battery materials with anisotropy > 1 MHz. *J. Am. Chem. Soc.* **134**, 1898–1901 (2012).
- 46 Sananes, M., Tuel, A., Hutchings, G. & Volta, J. Characterization of different precursors and activated vanadium phosphate catalysts by ^{31}P NMR spin echo mapping. *J. Catal.* **148**, 395–398 (1994).

- 1 47 O'dell, L.A., Rossini, A.J. & Schurko, R.W. Acquisition of ultra-wideline NMR spectra from
2 quadrupolar nuclei by frequency stepped WURST-QCPMG. *Chem. Phys. Lett.* **468**, 330–335
3 (2009).
- 4 48 Pell, A.J. *et al.* Frequency-stepped acquisition in nuclear magnetic resonance spectroscopy under
5 magic angle spinning. *J. Chem. Phys.* **138**, 114201 (2013).
- 6 49 Massiot, D. *et al.* ^{71}Ga and ^{69}Ga nuclear magnetic resonance study of $\beta\text{-Ga}_2\text{O}_3$: resolution of four-
7 and six-fold coordinated Ga sites in static conditions. *Solid State Nucl. Magn. Reson.* **4**, 241–248
8 (1995).
- 9 50 Mccloskey, B.D. *et al.* Solvents' critical role in nonaqueous lithium–oxygen battery
10 electrochemistry. *J. Phys. Chem. Lett.* **2**, 1161–1166 (2011).

11

12

Competing interests

The authors declare no competing interests.

Figure legends

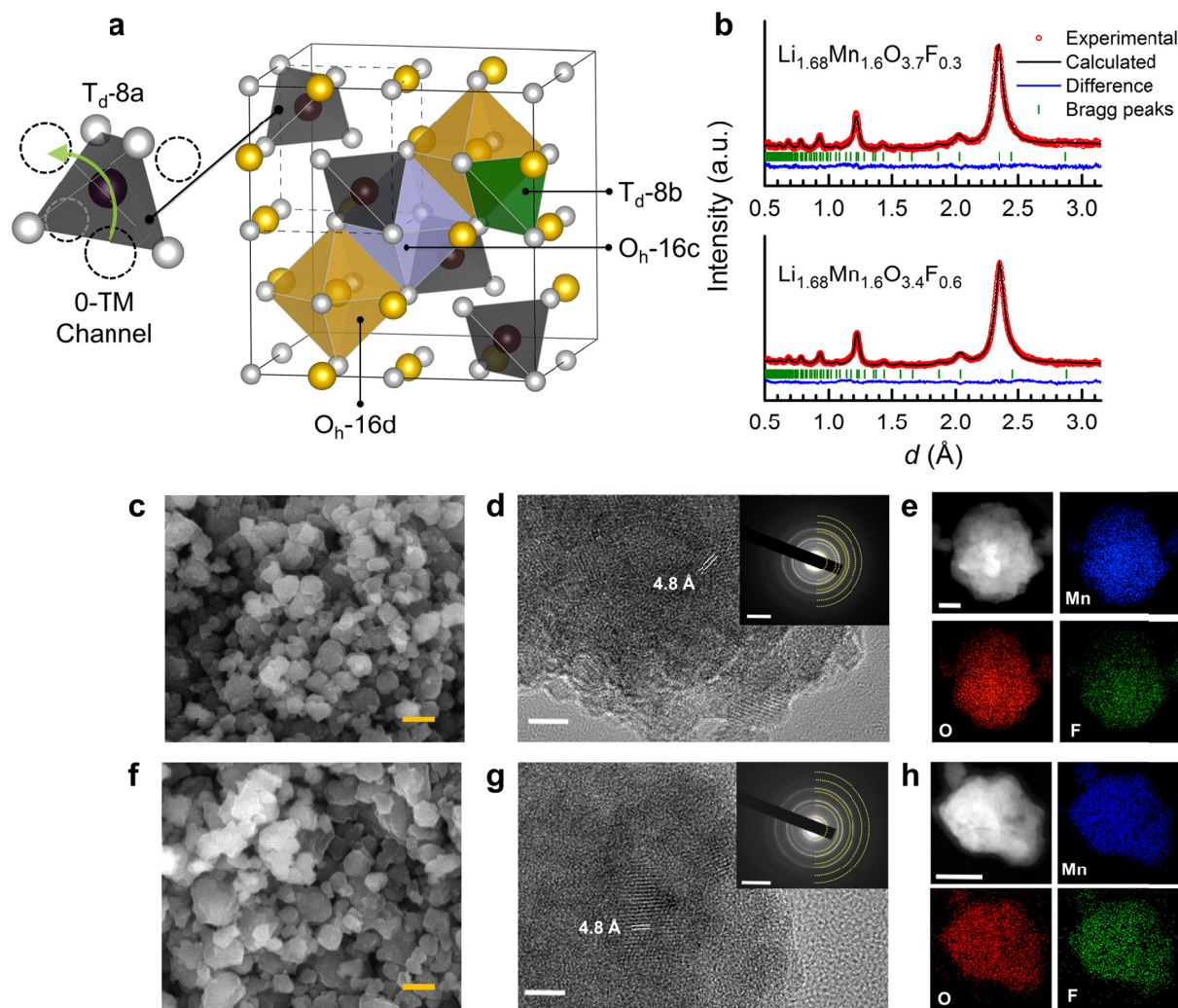


Figure 1. Structural and morphological characterization of two oxyfluorides LMOF03 and LMOF06. **a.** Crystal structure fragment of a perfectly ordered spinel LiM_2O_4 , with the high-symmetry Wyckoff positions T_d-8a , T_d-8b , O_h-16c , O_h-16d highlighted as colored polyhedra. A pseudo face-centered cubic anion framework is outlined with black dashed lines. The black, yellow and silver spheres represent the occupying Li, M and F/O atoms, respectively. One T_d-8a

1 site is enlarged to illustrate a 0-TM channel, in which none of its four face-sharing octahedral
2 sites (dashed circles) is occupied by TM. **b.** Rietveld refinement using time-of-flight neutron
3 diffraction data ($2\theta = 67^\circ$) at room temperature. **c,f.** SEM images of as-synthesized (c) LMOF03
4 and (f) LMOF06 (scale bars, 200 nm). **d,g.** HRTEM images (scale bars, 5 nm) and electron
5 diffraction patterns (scale bars, 5 nm^{-1}) of (d) LMOF03 and (g) LMOF06. The selected area
6 electron diffraction patterns can be indexed to a spinel lattice, with the d spacings determined to
7 be 4.8, 2.5, 2.1, 1.6, 1.5, 1.2, and 1.0 Å. **e,h.** EDS mapping of Mn, O and F in (e) LMOF03 and
8 (h) LMOF06 (scale bars, 50 nm).

9

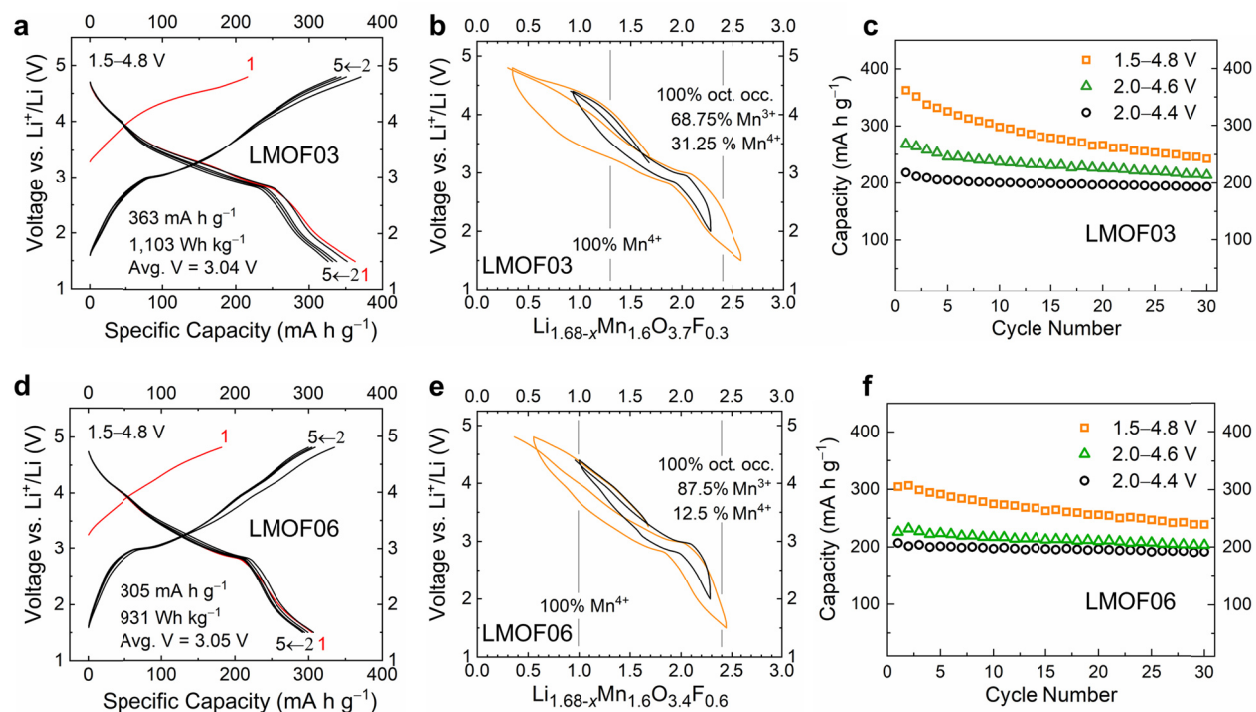


Figure 2. Galvanostatic charge and discharge performance of LMOF03 and LMOF06 at 50 mA g^{-1} at room temperature. a,d. Voltage profiles, started in charge, for the first 5 cycles obtained over the 1.5–4.8 V range, for LMOF03 and LMOF06, respectively. **b,e.** Voltage profiles during the first cycle and the second charge over voltage windows of 2.0–4.4 V and 1.5–4.8 V. **c,f.** Capacity retention over various voltage windows.

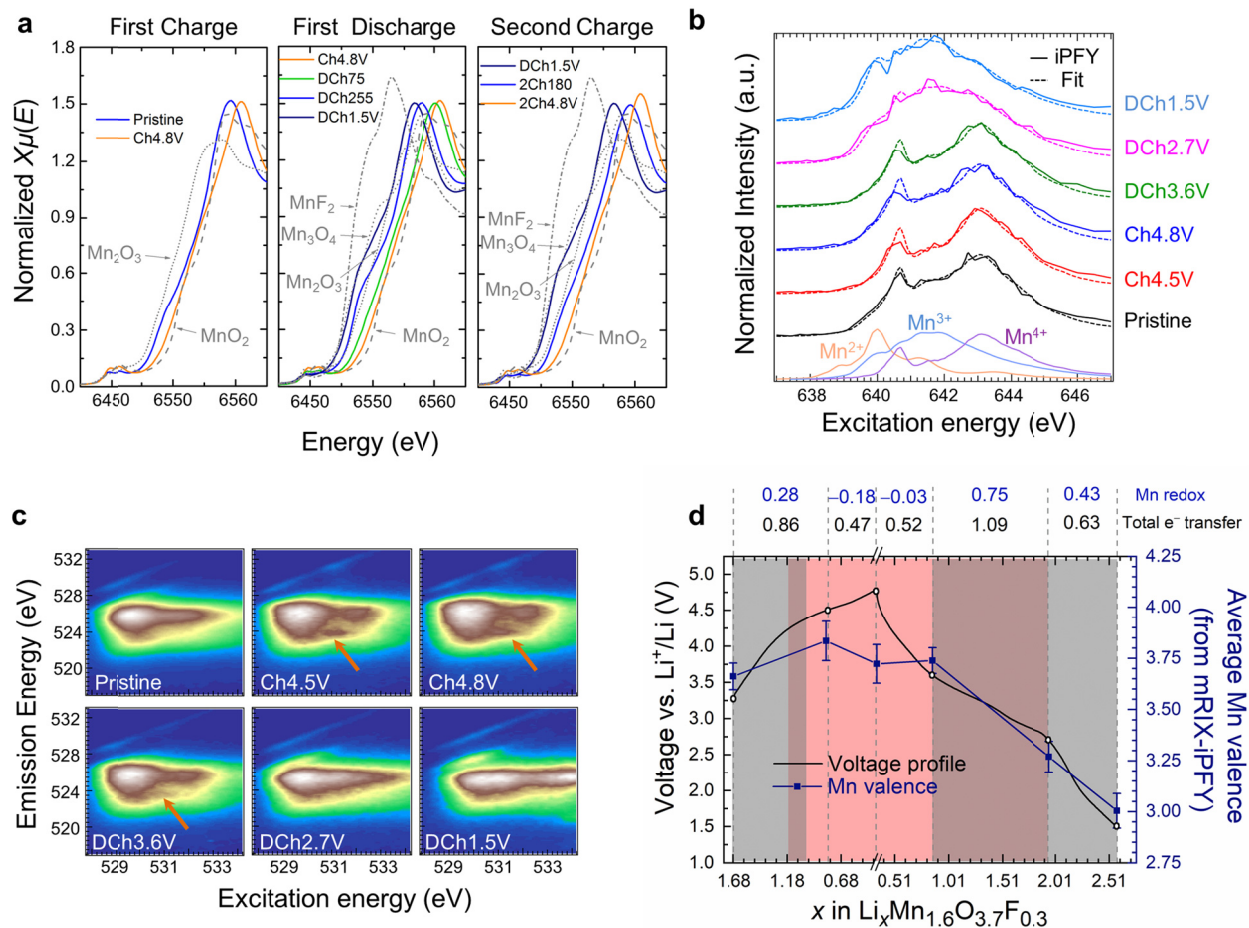


Figure 3. Redox mechanism of LMOF03. **a**, Operando Mn K-edge XANES spectra during the first charge-discharge cycle and second charge. The selected states are labeled by voltage or capacity. **b**, *Ex-situ* Mn L_3 -edge iPFY spectra extracted from Mn- L_3 mRIXS at six states of charge and discharge during the first cycle. Standard spectra of MnO , Mn_2O_3 , and MnO_2 are included as references. **c**, *Ex-situ* O K -edge mRIXS collected during the initial charge-discharge cycle. **d**, Quantification of Mn redox reactions during the initial cycle. The Mn valences obtained from a linear fit of the Mn- L_3 mRIXS-iPFY data at the six electrochemical states are plotted as navy squares. Each error bar represents the standard error calculated by combining the standard errors of the $\text{Mn}^{2+}/\text{Mn}^{3+}/\text{Mn}^{4+}$ fractions, which are obtained via linear fitting each Mn- L_3 mRIXS-iPFY spectrum. The numbers of total charge transfer and electron transfer from Mn

- 1 redox per f.u. over different voltage ranges are denoted in black and blue, respectively, above the
- 2 panel.
- 3

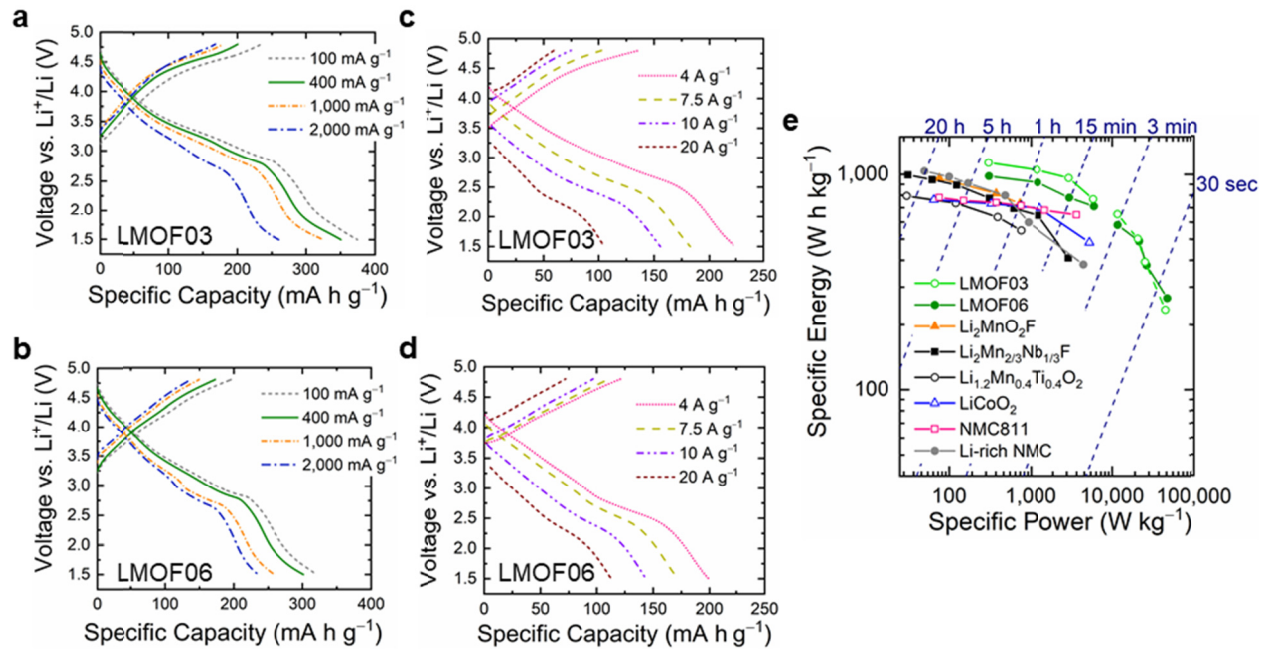


Figure 4. Rate capability measurements. Galvanostatic voltage profiles of (a,c) LMOF03 and (b,d) LMOF06 at various rates. A fresh cell was used for each rate test. e. Ragone plot comparing the specific energy and power of LMOF03 and LMOF06 to state-of-the-art Li-ion cathodes with optimized rate performance as reported in the literature [refs 5, 19, 32, 35–37]. The loading density of the cathode film is 2–3 mg cm⁻². The weight ratio of the active material, carbon black and Teflon in cathode films is 7:2:1 for rates from 100 to 2,000 mA g⁻¹, and 4:5:1 for rates from 4 to 20 A g⁻¹. The testing parameters for the cited materials are summarized in Supplementary Table 8.

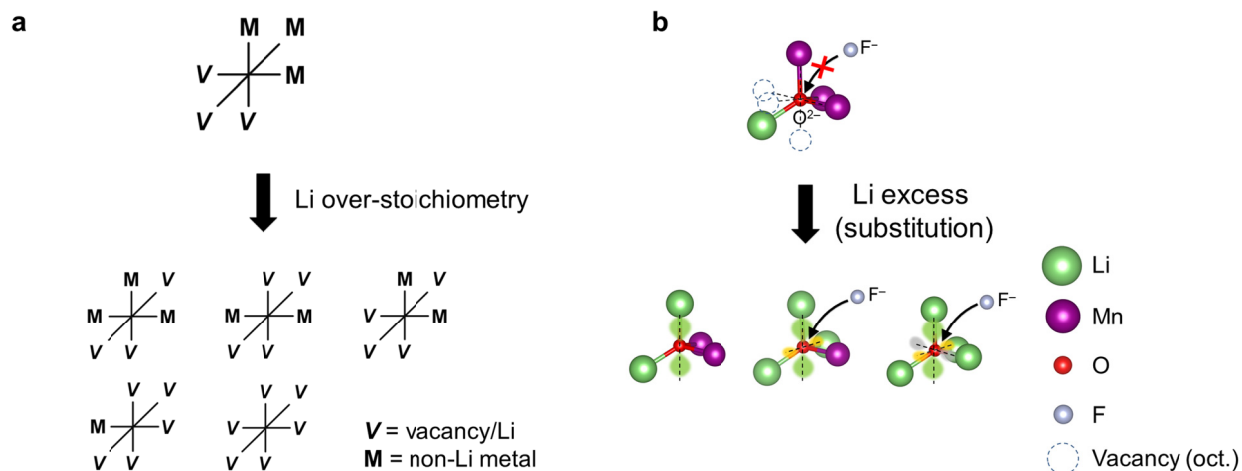


Figure 5. Illustration of partially (dis)ordered cation and anion local environments in a spinel-like structure that arise from Li over-stoichiometry and substitution. a. Diverse M configurations in an octahedral geometry around anions. M-richer cation arrangements are not shown given their low occurrence in the presence of over-stoichiometric Li. **b.** Change in the local bonding environment of anions from a stoichiometric spinel to a Li-excess spinel. The dumbbell-shaped clouds in green, yellow and grey schematically represent the unhybridized O $2p$ orbitals.